Tomographic velocity analysis and wave-equation depth migration in an overthrust terrain: A case study from the Tuha Basin, China

Bin Lyu[1], Qin Su[2], and Kurt J. Marfurt[1]

Abstract

Although the structures associated with overthrust terrains form important targets in many basins, accurately imaging remains challenging. Steep dips and strong lateral velocity variations associated with these complex structures require prestack depth migration instead of simpler time migration. The associated rough topography, coupled with older, more indurated, and thus high-velocity rocks near or outcropping at the surface often lead to seismic data that suffer from severe statics problems, strong head waves, and backscattered energy from the shallow section, giving rise to a low signal-to-noise ratio that increases the difficulties in building an accurate velocity model for subsequent depth migration. We applied a multidomain cascaded noise attenuation workflow to suppress much of the linear noise. Strong lateral velocity variations occur not only at depth but near the surface as well, distorting the reflections and degrading all deeper images. Conventional elevation corrections followed by refraction statics methods fail in these areas due to poor data quality and the absence of a continuous refracting surface. Although a seismically derived tomographic solution provides an improved image, constraining the solution to the near-surface depth-domain interval velocities measured along the surface outcrop data provides further improvement. Although a one-way wave-equation migration algorithm accounts for the strong lateral velocity variations and complicated structures at depth, modifying the algorithm to account for lateral variation in illumination caused by the irregular topography significantly improves the image, preserving the subsurface amplitude variations. We believe that our step-by-step workflow of addressing the data quality, velocity model building, and seismic imaging developed for the Tuha Basin of China can be applied to other overthrust plays in other parts of the world.

Introduction

Although the structures associated with overthrust terrains form important targets in many basins, accurate seismic imaging remains challenging. There are often serious lateral velocity variations in overthrust belts, which lead to ray bending, resulting in time-migrated seismic images that are poorly focused images and mispositioned reflectors and diffracting edges. Depth migration is required to image complex overthrust structures with strong lateral velocity variations. Unfortunately, the imaging problems are not confined to the deeper structures. Rough topography and outcropped older, high-velocity rocks in overthrust belts (Alfonso and Guevara, 2004) often lead to seismic data contaminated by headwaves and coherent backscattered noise resulting in a low signal-to-noise ratio (S/N) and serious statics problems, which complicate the velocity model building process critical to accurate depth migration. Alfonso (2001) identifies three major challenges in overthrust imaging: topography and its correction, the lower S/N associated with structure outcropping on the surface, and complex subsurface structures.

Other authors have addressed the rough topography and change in elevation encountered in overthrust belt imaging. Reshef (1991), Gray and Marfurt (1995), and Shragge (2005) find that depth migration directly from topography provided more accurate images compared with those computed from a flat datum after static corrections. However, the velocity model building difficulty remains, with a key challenge being how to integrate the near-surface velocity model computed from refracted waves with the deeper velocity model computed from reflected waves. Static correction plus migration from a floating datum provides a practical, but only partial, solution to this difficult problem. Yilmaz (2001) summarizes several static correction solutions, including field statics, refraction statics (Schneider and Kuo, 1985; Taner et al., 1998), and tomostatics (Zhu et al., 1992, 1998; Bell et al., 1994; Osypov, 1998). Accurate refraction statics computation requires continuous refractors and good

[1]The University of Oklahoma, ConocoPhillips School of Geology and Geophysics, Norman, Oklahoma, USA. E-mail: bin.lyu@ou.edu; kmarfurt@ou.edu.

[2]Petrochina Research Institute of Petroleum Exploration & Development-Northwest, Lanzhou, Gansu, China. E-mail: suq@petrochina.com.cn.

Manuscript received by the Editor 13 March 2017; revised manuscript received 19 July 2017; published ahead of production 19 September 2017; published online 14 November 2017. This paper appears in *Interpretation*, Vol. 6, No. 1 (February 2018); p. T1–T13, 13 FIGS.

http://dx.doi.org/10.1190/INT-2017-0053.1.

data, but it often fails when the data are poor or when the refracting horizons are discontinuous. Overthrust belts exhibit different types of topography, with a weathering zone occurring at lower elevations and outcrops at higher elevations, with no continuous refractor running across the entire survey. Such a near-surface problem cannot be solved well with only one static correction method.

Wang et al. (2012) identify several types of noise common to overthrust belts. Older and more indurated rocks outcrops give rise to high-amplitude headwaves, backscattered energy, and other linear noise, which overprints the reflections of interest. Such noise makes velocity model building much more difficult because the linear noise masks the reflections in common-image gathers and gives rise to semblance anomalies that may introduce incorrect velocity picks.

Ritchie et al. (2005) note the significant structural distortion due to severe thrusting or compression in overthrust belts. The structures in these areas are often very complicated and give rise to serious lateral velocity variations. Compared with lower cost Kirchhoff migration and higher cost reverse time migration (RTM), one-way wave-equation migration (Claerbout, 1971; Stoffa et al., 1990; Ristow and Ruhl, 1994) provides a practical solution to overthrust imaging, providing the multipathing benefits of a wave-equation method but at a reduced cost and somewhat reduced sensitivity to velocity errors than RTM. Although Jiao et al. (2004) apply this technique to synthetics and Shragge (2005) to field data, one-way wave-equation solutions face challenges in accurately accounting for topography and high velocities near the surface overlying slower velocities at depth, thereby filtering out shorter wavelength components representing steeper dips to make the algorithm stable.

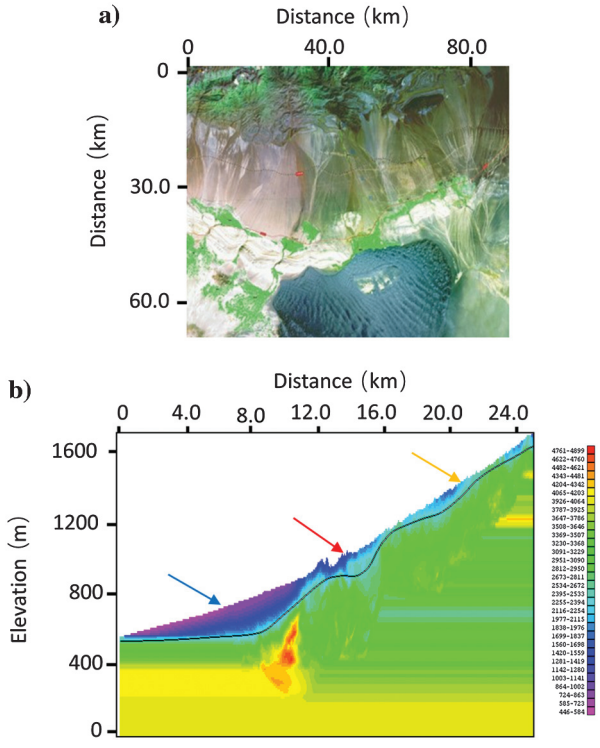

Figure 1. (a) The surface photograph and (b) the near-surface model built using a tomographic method of our research survey in the overthrust belt of the Tuha Basin, China. They indicate serious elevation variations from approximately 500 to 1700 m above the sea level, and they illustrate different types of the near surface, including the relatively flat Gobi desert covered with coarse gravels (blue arrow), the mountain front transition zone (red arrow), and the mountain outcrop area with high-velocity carboniferous rocks (orange arrow).

Constructing an accurate velocity model is a key to accurate depth imaging in an overthrust belt. For the areas with relatively simple structures and high-S/N data, layer-based coherency inversion (Yilmaz, 2001), or simple conversion of stacking velocities (Dix, 1955) can provide an initial interval velocity model. After constructing the first pass of (approximately flattened) migrated gathers, one can use tomography to update the velocity model (Etgen, 1988; Stork, 1992). However, these methods often fail where rocks outcrop at the surface and where the S/N is low. In this case, geologic information needs to be incorporated as well to build a more accurate depth-domain velocity model.

We begin our paper by building a synthetic wave equation model to better evaluate the quality of the seismic images from the prestack time- and depth-migration methods. We then introduce the depth-imaging workflow to be used in the overthrust belt. Next, we indicate the benefit of tomography in addressing statics issues associated with near-surface or outcrop high-velocity rocks. We address the S/N through a multidomain noise attenuation workflow. We then apply an amplitude-preserved one-way depth migration that compensates for lateral variation in wave illumination. Finally, we integrate additional velocity information from geologic outcrops to constrain our depth-domain velocity model, thereby improving our images. We conclude with summary comments and recommendations for further analysis.

Time imaging or depth imaging?

Although laterally variable from image point to image point, the velocity model for time migration at a given image point is either constant or a simple gradient of the form $v = v_0 + kz$, such that there is no ray kinking. In contrast, the velocity model for depth migration attempts to approximate the true layer-by-layer interval velocities with ray bending and kinking at each abrupt change in the velocity-depth model (Gray et al., 2001). In time migration, the imaging velocity model often begins with the root-mean-square (rms) velocity computed from unmigrated CMP gathers, which is then scaled to obtain the best focusing at every output location (Gray et al., 2001). Because there are no lateral velocity variations to focus the energy at a given image point, there is no need for explicit ray tracing, such that time migration is much faster than depth migration. If there are significant lateral velocity variations that give rise to ray bending, time migration not only laterally mispositions a given dipping seismic event, but it may also

separate or overlap adjoining parts of what should be a continuous reflector.

The velocity model used in depth migration is a smoothed representation of the true interval velocity, where for Kirchhoff migration, the smoothness is on the order of a wavelength (Gray et al., 2001), but it can be less for the one-way wave equation and RTM algorithms. All three of these implementations (ray-based, one-way wave-equation, or hyperbolic two-way wave equation) algorithms accurately bend the rays at each location in the subsurface where the velocity changes, such that depth migration can image complicated subsurface structures much more accurately than time migration can.

In our study, we perform the numerical tests on a land survey with overthrust structures of the Tuha Basin. The survey exhibits complicated subsurface structures and rugged topography. Figure 1a shows the surface photograph that covers our survey, which indicates very complex near-surface conditions. Figure 1b shows the near-surface model built using a tomographic method, which indicates serious elevation variations from approximately 500 to 1700 m above sea level. Figure 1a and 1b also illustrates different types of the near surface, including the relatively flat Gobi desert covered with coarse gravels (blue arrow), the mountain front transition zone (red arrow), and the mountain outcrop area with high-velocity carboniferous rocks (orange arrow).

Although some pitfalls of time migration, such as velocity pull up/push down (e.g., Fagin, 1996) are well-known to interpreters working on overthrust terrains, we reveal these phenomena by constructing the model shown in Figure 2b based on the depth-domain structural interpretation (Figure 2a) of a typical line in the overthrust belt shown in Figure 1. There are a shallow overthrust structure and some underlying faults in the model. We then generate a suite of common-shot synthetics using a 2D finite-difference scalar wave-equation algorithm. The time-processing steps prior to migration are similar to those applied to the field data. Figure 2c and 2d shows the resulting prestack time- and depth-migrated images. Note the improved fidelity of the depth-migrated image compared with the true model. Faults are accurately imaged to their correct location in depth migration, but they are distorted and mispositioned by time migration. There are strong fault shadow effects on the deepest two reflectors (yellow arrows) in the prestack time-migration image, which are caused by the rapidly varying lateral velocity contrast across the dipping faults. These reflections are nonhyperbolic around the faults, resulting in weak time-migrated images. It is difficult to image these dipping fault zones with prestack time migration (Figure 2c), due to its inability to handle lateral velocity variations. The fault-plane reflection is also mispositioned with prestack time migration (blue arrows). In contrast, prestack depth-migration images these fault zones much better (Figure 2d). There are fewer migration artifacts in depth imaging, with the pull-up artifacts removed. Multiples are more coherent, but they are easier to identify as being multiples on the prestack time-migrated volume, indicated by the red arrows in Figure 2c. On the depth-migrated data, the multiples are weaker, but they are no longer periodic, and they may be misidentified as primaries on the prestack depth-migrated data volume (red arrow in Figure 2d).

The primary processing steps of the workflow are shown in Figure 3. Other steps, such as geometry definition, first-break picking, muting, and velocity picking also affect the imaging quality. There are four key steps for depth imaging in the overthrust belt: static corrections, noise attenuation, the prestack depth migration algorithm, and depth-domain velocity model building. Each will be discussed in detail in the following subsections.

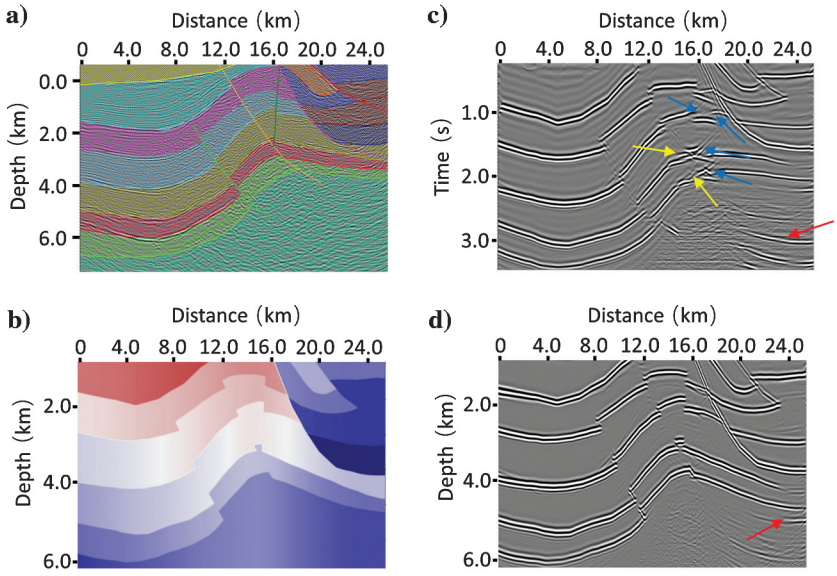

Figure 2. A synthetic model built from the image of the Tuha Basin to quantify any limits in imaging the overthrust structures. (a) Depth-domain structural interpretation of a typical line of our research survey. (b) Velocity-depth model used to generate acoustic wave equation synthetic shot gathers using a finite-difference algorithm. Resulting images from (c) prestack time migration and (d) prestack depth migration. Note the strong fault shadow effects on the deepest two reflectors (yellow arrows) on the prestack time migration. Prestack depth migration could image these fault zones much better. The fault-plane reflection is also mispositioned with prestack time migration (blue arrows). There are fewer migration artifacts in depth imaging, and the pull-up pitfall is also removed in depth imaging. In contrast, the multiples are more coherent, but they are easier to identify as being multiples on the prestack time-migrated volume. Although the multiples are weaker, they may be misidentified as being structures on the prestack depth-migrated data volume (red arrows).

Computing the near-surface velocity model

Properly accounting for elevation and weathering zone effects is critical for land processing (Yilmaz, 2001), and it is more challenging in areas with rough topography, such as in overthrust terrains. The Tuha Basin expresses variable topography, including flat plains and desert, the mountain front, and the mountains themselves. In most land surveys, the seismic data are recorded by geophones deployed on the surface of a low-velocity weathering zone. Energy impinging the base of the weathering zone at shallow angles is refracted toward the normal, which for relatively flat topography and weathering zones, toward the vertical, such that the weathering zone correction can be approximated by a vertical (static) shift of the seismic trace. In the case of rough topography, the surface and the base of the weathering zone may not be flat. In some cases, such as in the Tuha Basin overthrust belt, there is no weathering zone at all, but rather the folded rocks outcrop at the surface.

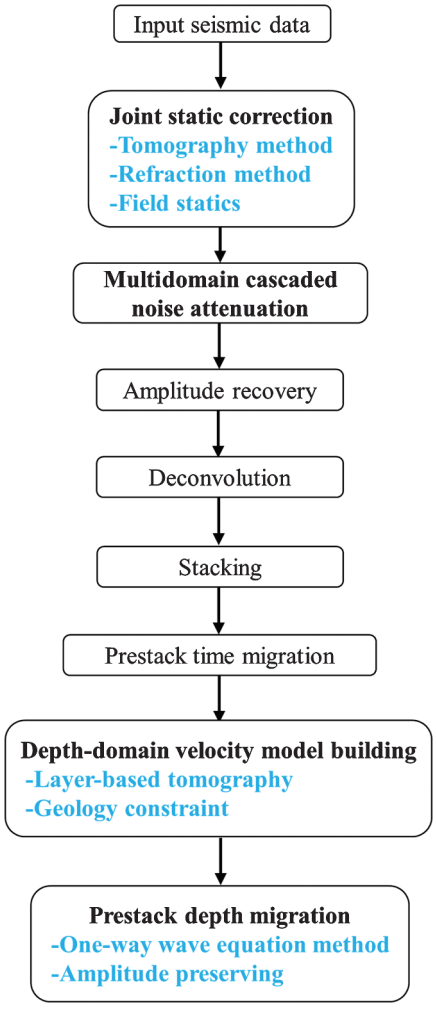

Figure 3. The seismic processing workflow in the overthrust belt indicate the four key steps for seismic imaging in the overthrust belt, including statics correction, noise attenuation, prestack depth-migration algorithm, and depth-domain velocity model building.

In this case, there is no bending of raypaths toward the vertical because they approach the surface. Taner et al. (1974) show that correcting these measurements to a flat datum requires a "dynamic" rather than a "static" correction, whereby each reflection event needs to be corrected to the data by its angle of incidence back to the datum along the raypath, rather than vertically. Reshef (1991), Gray and Marfurt (1995), and Shragge (2005) show that migration directly from topography implicitly computes such a dynamic correction, providing significantly more accurate images than the migration of data previously corrected to a flat datum using static corrections.

Although migration from topography has been available for decades, estimating an accurate velocity in the low-fold shallow section is still difficult in the Tuha Basin survey, refraction statics velocity analysis based on smooth, continuous refractors fails. Furthermore, the velocity field estimated from shallow refractions and that estimated from deeper reflections have different scales, making their integration into a unified velocity-depth model difficult.

Rough topography can be considered to have low- and high-frequency components. The floating datum represents the low-frequency component, which could also be considered to be a smoothed version of topography. For the Tuha Basin overthrust data, we use a two-step correction: First, we correct the high-frequency component to a floating data, followed by migration from the floating datum. By this, the inaccurate vertical correction to a flat datum is minimized, whereas the data can be regularized to a grid, in which the one-way wave-equation solutions can operate.

Yilmaz (2001) summarizes several different static correction methods to correct the high-frequency component of topography, including field statics, refraction statics (Schneider and Kuo, 1985; Taner et al., 1998), and tomostatics (Zhu et al., 1992; Bell et al., 1994; Osypov, 1998). Refraction statics works well for continuous refractors and good-quality data, but it may fail in the presence of discontinuous refractors and poor-quality data.

The Tuha Basin overthrust belt is represented by significant lateral variations in the near-surface structures. In our research area, the near-surface changes from the Gobi Desert through a mountain front transition zone, followed by the mountain outcrop area (Figure 1b). The Gobi Desert is relatively flat with small elevation variations. In the mountain front transition zone, the elevation variations become larger, but there is still a stable refraction layer. The mountain outcrop area exhibits serious lateral variations, and there are no stable refraction layers.

Given the heterogeneity, no single static correction technique works for the entire line. We illustrate our hybrid static correction workflow using a representative line drawn from the survey shown in Figure 4. Three different static correction methods, including field statics, refraction statics, and tomostatics, are used for numeri-

cal tests. Figure 4a, 4d, and 4g shows the imaging results in the Gobi desert area after static correction with these three different methods. In this area, the topographic variation is relatively small and there are abundant micrologging and shallow refraction data in our survey, resulting in an accurate image using the conventional field static correction method (Figure 4a).

The comparative results for the mountain front transition belt are indicated in Figure 4b, 4e, and 4h. There are stable refraction layers (Figure 1b) in this area and the data quality is relatively high, which satisfy the requirement of the refraction method. The resulting image using refraction statics (Figure 4e) is better than those using the other two methods (Figure 4b and 4h).

Figure 4c, 4f, and 4i shows the three results in the mountain area with outcropped structures. Refraction layers are absent, and the data quality is relatively poor. In this area, the refraction method fails to produce a good image (Figure 4f). In contrast, a tomographic solution provides a significantly improved image (Figure 4i) over the two other methods.

Because tomographic statics provides a more continuous shallow reflector (yellow arrow) and higher resolution deeper reflector (orange arrow), refraction statics provides a more continuous reflector at depth for the mountain front example (red arrow), and field statics provides more continuous reflectors in the Gobi Desert example (blue arrow), we construct a hybrid method that uses each static correction where it works best. We integrate the three solutions using cokriging interpolation to obtain an optimum static correction spanning the different types of topography.

Multidomain seismic noise attenuation

Wang et al. (2012) report that land surveys acquired over overthrust structures such as those of the Tuha Basin are contaminated by multiple types of noise, including backscattered ground roll and high-velocity shallow refractions. The S/N is exacerbated when older, more indurated rocks outcrop, giving rise to high-velocity, poorly attenuated ground roll, and high-amplitude head waves that exhibit similar velocities to the vertically traveling reflections. If aliased, such noise overprints subsequent depth imaging with artifacts, masking reflections and diffractions of interest (Marfurt and Duquet, 1999). When stronger than the reflections, the noise renders velocity analysis more difficult and prone to event mispicks, resulting in an inaccurate velocity-depth model.

For the Tuha Basin survey discussed here, noise could not be adequately suppressed in either the common-midpoint or common-shot domain. For this reason, we follow the workflow described by Vermeer (1991) that suggests cascaded filtering, first in the common-shot domain (which allows suppression of noise radiating away from the shot) followed by the common-receiver domain (which allows suppression radiating toward the receivers). The latter noise trains include not just remnants of the previously suppressed shot to receiver ground roll and headwaves, but also backscattered energy from surface topography and irregular weathering zones.

Figure 5a shows a representative common-shot gather, in which strong linear noise masks the underlying signal. This noise leaks through the stack array indicated by the yellow arrows in Figure 5e. In our research, the linear noise is suppressed with an f-k filtering method (Yilmaz, 1987; Zhou and Greenhalgh, 1994). The linear event function u in the t-x domain can be expressed as

$$u(x,t) = s(t) * \delta(t - x\,\tan(\alpha) + b), \tag{1}$$

where $s(t)$ is a band-limited wavelet, b is the intercept of the linear event on t-axis, and α is the angle between the linear event and x-axis. We transform the input seismic data $u(x,t)$ from the t-x domain to the f-k domain:

$$\begin{aligned} U(k,\omega) &= S(\omega)\exp(i\omega b)\delta(k - \omega\,\tan(\alpha)) \\ &= S(\omega)\exp(i\omega b)\delta(\omega - k\,\cos(\alpha)), \end{aligned} \tag{2}$$

where $U(k,\omega)$ and $S(\omega)$ are the Fourier transform of $u(x,t)$ and $s(t)$. The linear noise will be suppressed

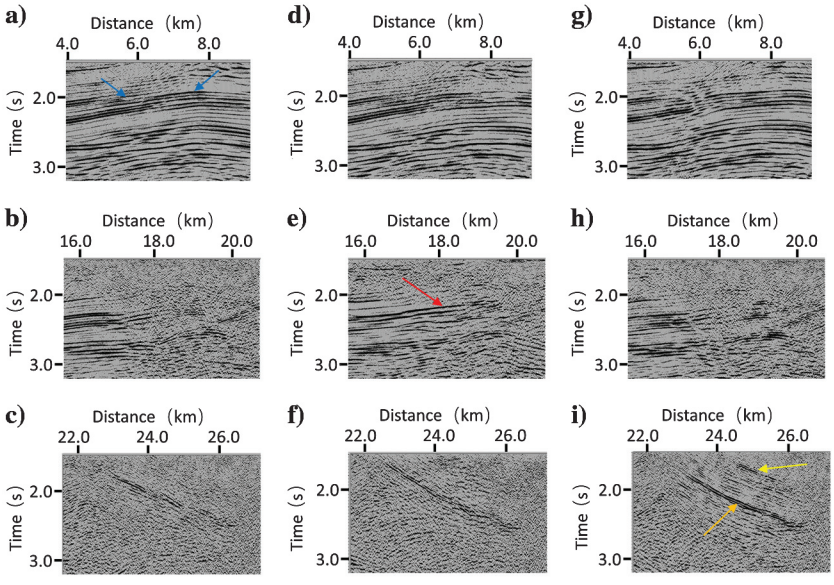

Figure 4. The effect of alternative statics solutions on the final depth-migrated images for the overthrust belt, Gobi Desert, and mountain front field data examples. Tomographic statics (i) provides a more continuous shallow reflector (yellow arrow) and higher resolution deeper reflector (orange arrow) than does (f) refraction statics or (c) field statics for the overthrust belt. (e) Refraction statics provides a more continuous reflector at depth for the mountain front example (red arrow) than does (h) tomographic statics or (b) field statics. In contrast, (a) field statics provides more continuous reflectors in the Gobi Desert example (blue arrow) than does (d) refraction statics or (g) tomographic statics.

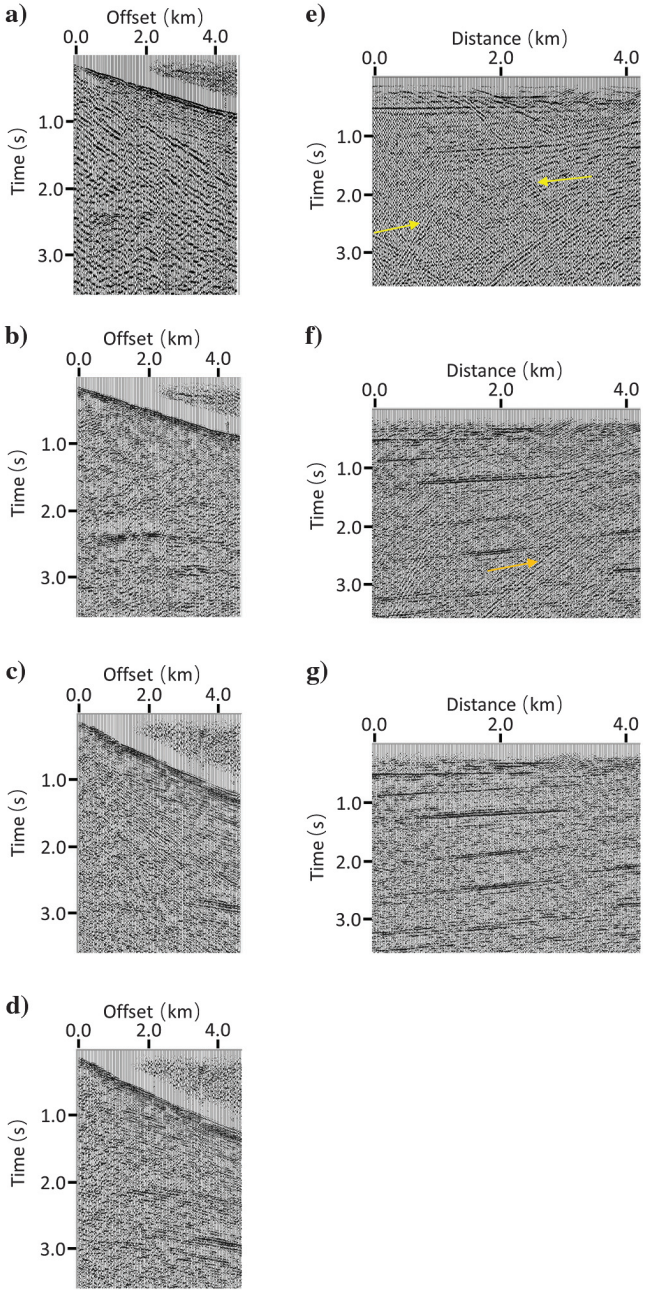

Figure 5. The results of multidimensional suppression of linear noise in the overthrust example. A representative common-shot gather (a) before and (b) after linear noise attenuation. (c) The rejected linear noise reappears when sorting the previously filtered data into the common-receiver gather. (d) The same common-receiver gather shown in (c) after a second pass of linear noise attenuation on common-receiver gather. Stacked images of (e) the original unfiltered data, (f) after linear noise suppression only in the common-shot domain, and (g) after linear noise suppression in the common-shot and common-receiver domain. Note that the linear noise in both directions leaks through the stack array (yellow arrows). Although it is suppressed, linear noise still leaks through after filtering common-shot gathers (orange arrow). Sequential filtering of common-shot gathers followed by common-receiver gathers significantly reduces the noise in the stack shown in (g).

according to their dips in the f-k domain. Figure 5b shows the same shot gather after linear noise attenuation using the f-k filter. Although there is little noise on the resulting gather, after stack the linear noise reappears indicated by orange arrows in Figure 5f. Resorting the f-k filtered common-shot gathers to common-receiver gathers shows that significant linear noise remains (Figure 5c). Application of a second pass of f-k filtering in the common-receiver domain suppresses this noise component (Figure 5d). Two passes of f-k filtering, first in the common-shot domain and then in common-receiver domain, results in the stacked section shown in Figure 5g, in which one sees that the cascaded filter significantly reduces the noise in the stack, allowing the reflectors to show through.

Figure 6 shows how multistep linear noise attenuation works. There are several families of linear noise events, each with a different velocity seen on the raw common-shot gather (Figure 6a). The linear noise with low and high velocities exhibit different amplitudes. In principle, if one can identify all noise events, one can suppress them simultaneously in the f-k domain. In practice, this is difficult, with the high-amplitude noise masking the low-amplitude noise. Therefore, we apply an f-k filter to suppress the stronger low-velocity linear noise indicated by the yellow arrows (Figure 6b) first. Next, we applied a second f-k filter to suppress the higher velocity noise indicated by the blue arrows (Figure 6c). Although the high-velocity linear events are effectively suppressed, aliased components of the low-velocity events, including ground roll (red arrows), have leaked through the filter. These remnant "shingled" events indicated by the green arrow exhibit a high apparent velocity and will be migrated as "signal" into the final image, damaging the overall S/N and interpretability of the section.

Wave-equation depth migration with illumination compensation

Etgen et al. (2009) divide depth migration into ray-based and wave-equation-based methods. Kirchhoff depth migration (Schneider, 1978; Bleistein, 1987) is the most popular ray-based method, and it still plays an important role in seismic imaging and migration velocity model building. Ray theory, and therefore Kirchhoff depth migration, is based on a high-frequency approximation, in which the seismic wavelength is much shorter than the scale of velocity changes. One can either sum events in depth along diffraction traveltime curves or distribute events along deformed ellipsoids to generate an output image. Because Kirchhoff depth migration is based on a high-frequency, asymptotic solution of wave equation, it does not accurately account for low-frequency phenomena such as geometric scattering and dispersion, caustics, and tunneling in the downgoing and upcoming raypaths. A larger limitation is due to implementation rather than theory. For reasons of algorithmic complexity, most software allows only a single raypath, and hence computes only one traveltime, to represent

the path from a surface source or receiver to the subsurface image point. Nevertheless, Kirchhoff depth migration has several benefits. First, compared with wave-equation methods, the computation cost of Kirchhoff depth migration is less, comprising precomputation of a suite of traveltime tables, which can be generated either by a simple ray-shooting method, wavefront extrapolation, or finite-difference solutions of the eikonal equation, followed by summation of the data along the two-way traveltime curves. Second, Kirchhoff depth migration has great flexibility. One can migrate directly from topography and limit the output to a subset number of laterally or vertically targeted subset of the earth. This latter capability is critical for migration velocity model building, in which one wishes to iterate only those parts of the model that need velocity updating. Although the ability to image sources and receivers where they are deployed is an advantage, it is also a disadvantage if the processor naively ignores operator aliasing resulting in artifacts overprinting reflectors of interest (Gray et al., 2001).

In contrast, wave-equation depth-migration algorithms implicitly include multipathing between any surface location and the image point of interest. Imaging through caustics and through more rugose interfaces requires no extra software; rather, wave phenomena are implicitly accounted for. Wave-equation solutions require the data to be resampled on a regular grid, typically with constant "receiver" spacing, requiring premigration data sampling and interpolation. This extra layer of complexity forces the processor to deal directly with the seismic aliasing problem that may be overlooked when using the more flexible Kirchhoff depth-migration algorithm.

Wave-equation migration includes one- and two-way methods. The two-way RTM method (Hémon, 1978; Baysal et al., 1983; McMechan, 1983; Whitmore, 1983) is based on the full two-way wave-equation solution, rather than on an asymptotic solution, which leads to higher imaging precision compared with other migration methods. However, it is much more time consuming, requires greater computer memory, and exhibits greater sensitivity to velocity errors compared with other depth-migration methods (Shan et al., 2008). In contrast, the computationally more efficient one-way

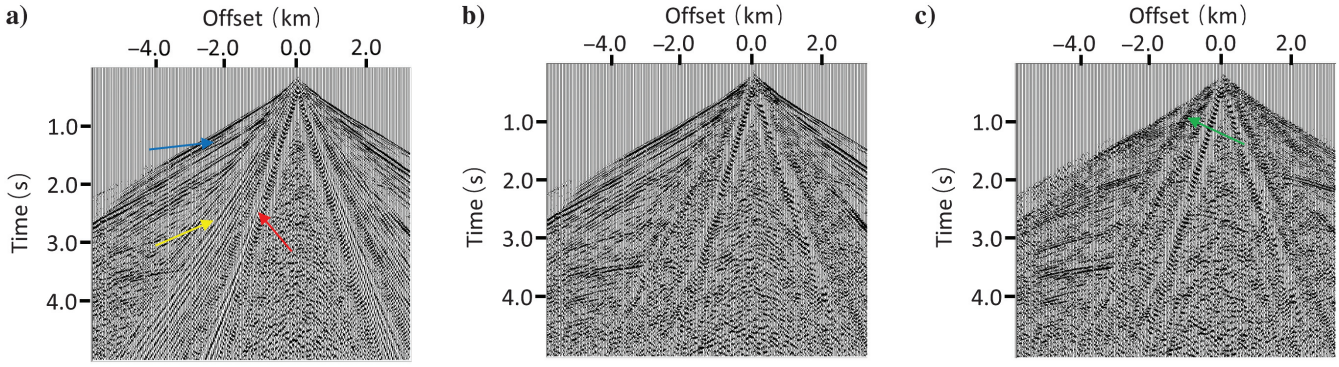

Figure 6. Multistep linear noise attenuation for the overthrust belt example. (a) A representative common-shot gather exhibiting high-velocity noise (blue arrows), low-velocity noise (yellow arrows), and ground roll (red arrows). The same gather after linear noise suppression of the (b) low-velocity linear events and (c) high-velocity linear events. Although the high-velocity linear events are effectively suppressed, aliased components of the lower velocity events, including ground roll, have leaked through the filter. The shallow apparent dips (green arrow) of these events will be migrated as signal into the final image, damaging the overall S/N and interpretability of the section.

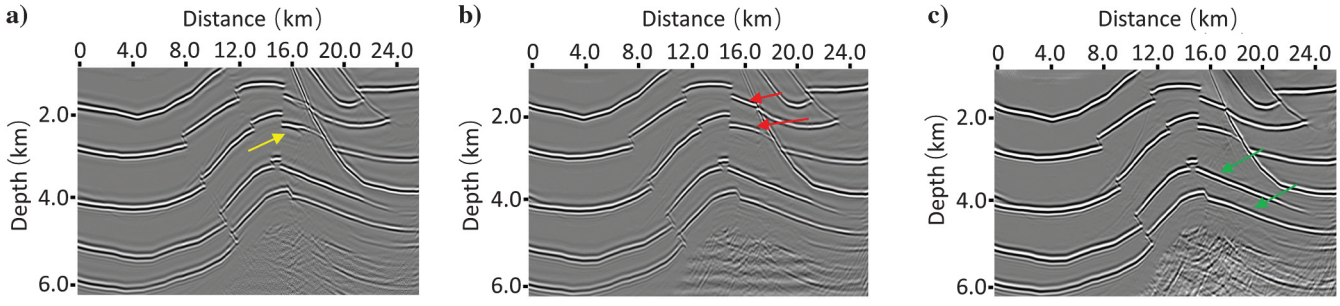

Figure 7. Comparison of different depth-migration methods on the overthrust synthetic data of Figure 2. (a) Kirchhoff depth migration, (b) conventional one-way wave-equation depth migration, and (c) amplitude-preserved one-way wave-equation depth migration. Low-frequency artifacts creep into the Kirchhoff depth-migrated image indicated by yellow arrows, but they are largely suppressed in the one-way wave-equation image. The underlying reflectors have poor images due to the overlying high-velocity structures in the Kirchhoff migration, but they are effectively improved by the one-way wave-equation migration indicated by the red arrow. The amplitude-preserving algorithm more accurately represents the correct amplitude, especially for the deep reflectors indicated by the green arrow.

wave-equation depth-migration method (Claerbout, 1971; Stoffa et al., 1990; Ristow and Ruhl, 1994) has the advantages of multipathing and imaging through caustics of a wave-equation solution, but at a cost that allows for multiple iterations to determine the final velocity. In one-way wave equation depth migration, the full wavefield is divided into a downgoing wavefield and an upgoing wavefield. These two wavefields are extrapolated downward in depth rather than forward and backward in time as in RTM, thereby reducing the computer storage requirements to the solution at the current and next depth level. The accuracy of the one-way wave equation depth migration falls between that of Kirchhoff depth migration and RTM. The one-way wave equation accounts for multiple paths, so long as they are going in the direction of wavefield extrapolation, and it exhibits a lower sensitivity to velocity errors than does RTM.

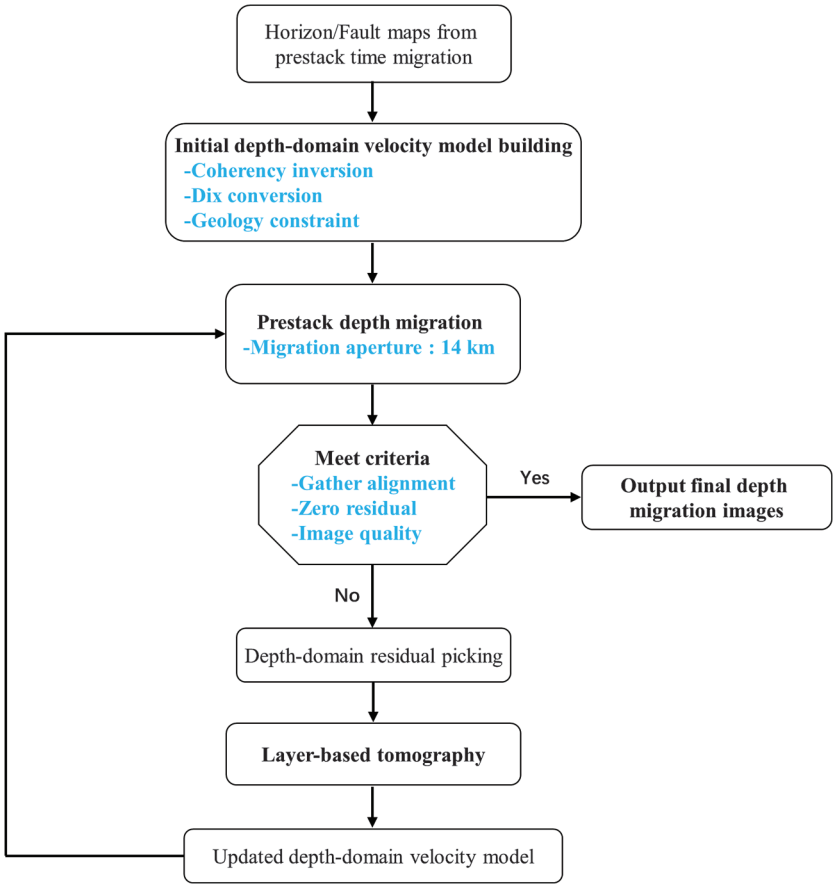

Figure 8. The prestack depth migration workflow in the overthrust belt, including the tomographic velocity updating procedure. Note that a large migration aperture is needed to image the steeply dipping reflectors and faults in the overthrust belt.

The key challenges of wave-equation depth migration on land data include data regularization, amplitude preservation, and velocity model building. Seismic data from land surveys sometimes are not well-sampled in different domains, with shot spacing often coarser than receiver group spacing. Prestack seismic gathers often exhibit "holes" due to surface "obstacles," which add additional artifacts to the subsurface image. In our research, seismic data regularization is carefully handled before migration in the f-x domain (Spitz, 1991). In this paper, we mainly focus on amplitude preservation and depth-domain velocity model building.

Older, more indurated rocks outcropping at or near the surface in overthrust terrains may have significantly higher velocities than the underlying strata. Unless they have flat interfaces, waves propagating through these zones may be strongly refracted away from the deeper target, leading to irregular subsurface illumination, giving rise to lateral changes in amplitude. After correction for spherical spreading and surface consistent amplitude corrections, we follow Zhang et al. (2005) and add amplitude recovery terms to the one-way wave-equation depth-migration algorithm that compensate for the lateral variation of illumination in depth. Figure 7 shows the comparison of different depth-migration

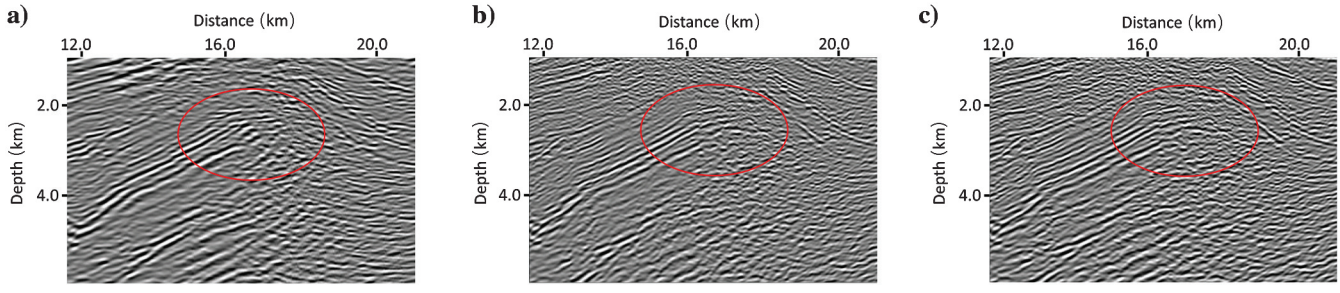

Figure 9. Comparison of different depth-migration methods on the field data with overthrust structures. (a) Kirchhoff depth migration, (b) conventional one-way wave equation depth migration, and (c) amplitude-preserved one-way wave-equation depth migration. The underlying faults are better imaged by the one-way wave-equation depth migration (red circle). The amplitude-preserving algorithm further compensates the imaging energy of the underlying reflectors.

methods on the synthetic data previously shown in Figure 2. Low-frequency artifacts creep into the Kirchhoff depth-migrated image indicated by yellow arrows in Figure 7a, but they are largely suppressed in the one-way wave-equation image (Figure 7b). The underlying reflectors are poorly imaged due to the overlying high-velocity structures in the Kirchhoff migration (Figure 7a), but they are well-imaged by the one-way wave-equation migration, indicated by the red arrow (Figure 7b). The amplitude-preserving algorithm (Figure 7c) more accurately represents the correct amplitude, especially for the deep reflectors indicated by the green arrow.

Figure 8 shows the prestack depth-migration workflow in the overthrust belt, including the tomographic velocity updating procedure. The migration aperture plays an important role in depth migration, especially for structures with steeply dipping reflectors and faults, such as overthrust structures. A much larger migration aperture is needed to image steep reflectors than flat reflectors. The larger migration aperture makes prestack depth migration more time consuming. The migration aperture (14 km) used in the survey shown in Figure 8 is much larger than the maximum source-receiver offset of 5.5 km, to image the steeply dipping structures. Figure 9 compares images from three different prestack depth migration methods, including Kirchhoff (Figure 9a), one-way wave equation (Figure 9b), and amplitude-preserved one-way wave equation (Figure 9c). The underlying faults are better imaged by the one-way wave-equation migration (Figure 9b and 9c) indicated by the red circle and arrow. The amplitude-preserving algorithm further compensates the imaging energy of the deep reflectors.

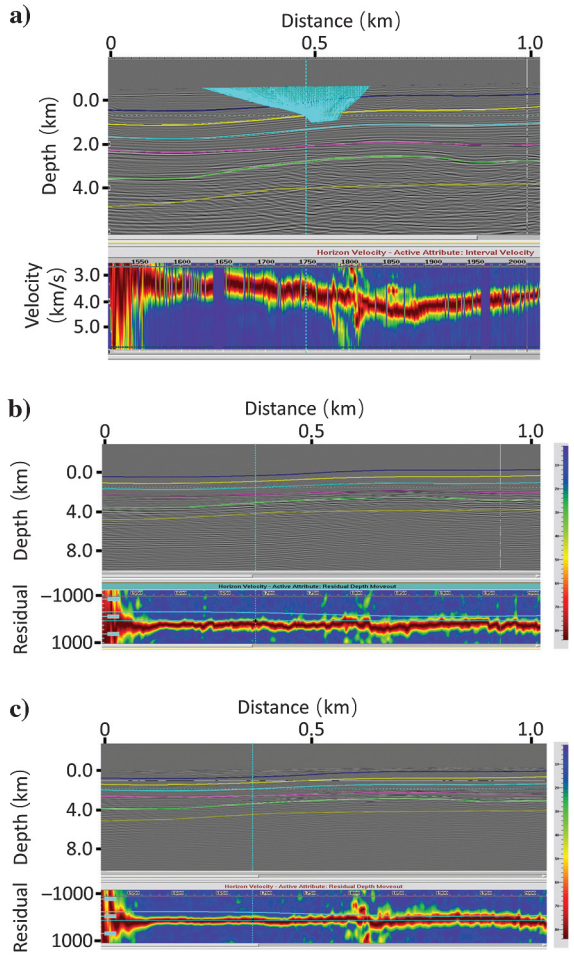

Figure 10. A comparison of alternative depth-domain velocity model building methods as measured by computing semblance scans across the migration gathers. For accurately migrated data, the gathers should be flat, showing a misalignment of zero. In contrast, areas that are overcorrected will have negative residual moveout, whereas those that are undercorrected will have positive residual moveout. Residual moveout computed from seismic images migrated using (a) Yilmaz's coherent event conversion result and (b) before and (c) after tomographic residual velocity correction.

Depth-domain velocity model building

Gray et al. (2001) report that if the velocity is correct and gives rise to ray bending, depth migration provides superior images than does time migration. In contrast, if the velocity model is inaccurate, time migration may provide a more focused (though laterally mispositioned) subsurface image.

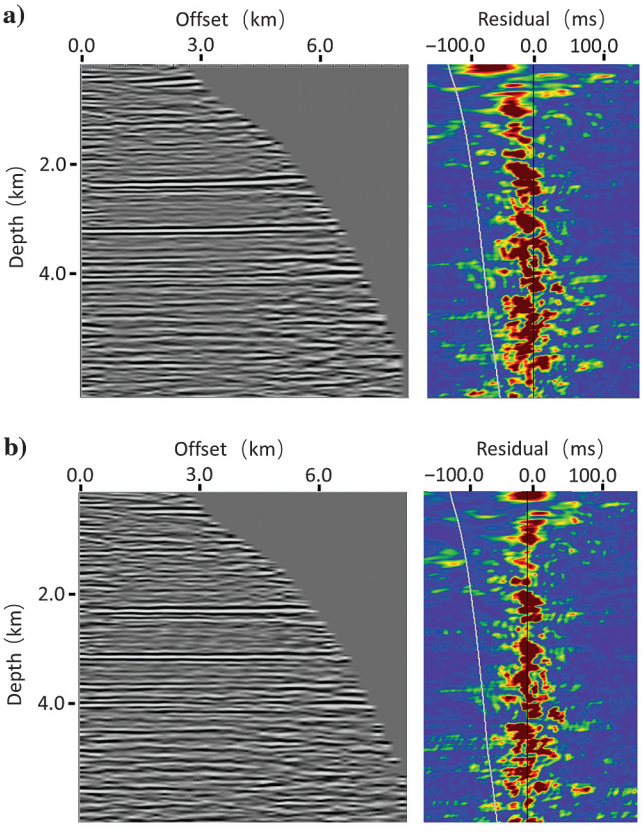

Figure 11. Comparison of common-image gathers located at lateral distance 14.0 km of Figure 9 (a) before and (b) after tomography. Note that the reflections behave upward with residuals before tomography, and they are aligned after tomography.

For the Tuha Basin survey, the shallowest component of the velocity model uses the previously described cokriging static correction to a floating datum. The reflection events are then used to construct the velocity model below the floating datum.

For the areas of the survey with relatively simple structures, no outcrops, and a high S/N, an initial model based on layer-based coherency inversion (Yilmaz, 2001) works well. This initial model is then updated using the tomography of the migrated gathers, iterating until the residual moveout approaches zero (i.e., the events are "flat"). The tomographic velocity updating workflow is included in Figure 8. In this study, we use a layer-based tomography method. Figure 10 shows the results of this workflow from the Gobi Desert area of the Tuha Basin survey. The shallower part of Figure 10a shows the interpretation of a prestack time-migrated result, exhibiting relatively simple structures and high data quality. The deeper part of Figure 10a was computed using coherency inversion, focusing the area interpreted by the light-blue horizon. This workflow provides a good initial velocity model with few artifacts. Figure 10b shows the residual about the light-blue layer horizon before tomography. After three iterations using the tomography method, the residual is better focused, converging toward zero, which is shown in Figure 10c. In Figure 11, we show the depth-domain common-image gathers located at $x = 14.0$ km in Figure 9. The reflections are overcorrected on the common-image gather without tomography, and there are obvious vertical residuals (Figure 11a). After tomography iterations, the reflections are aligned along the offset axis on the common-image gather and the vertical residuals are almost zero (Figure 11b).

There are plenty of faults and steeply dipping reflectors in our research survey, as shown in the representative seismic line in Figure 2. The underlying structures are important exploration targets in the Tuha Basin. However, the imaging of these structures is difficult due to the overlying outcropped rocks with very high velocities. Depth-domain interval velocity model building is critical for the imaging of these structures. Due to the complexity in these areas, the workflow for velocity model building in Figure 8 fails. The deeper part of Figure 12a shows the coherency inversion result of one layer in the overlying outcropped area. It is chaotic, making it difficult to pick accurate initial velocities. The simpler conversion of rms stacking velocities to interval velocities also fails. If the initial velocity model is too far from the correct velocity, the tomographic velocity updating workflow also fails.

Coherency inversion indicates three candidate velocity ranges. The lowest range is tightly clustered at approximately 2000 m/s. We consider this velocity to be unreasonably low for the older rocks in the Tuha Basin. Figure 12a shows the velocity model built with the middle range of velocities, without any geologic constraints. However, Figure 12b shows that the corresponding depth migration is of poor quality with crossing events, even after several iterations of tomography. The overlying outcropped rocks were measured directly and found to exhibit a very high velocity of approximately 5000 m/s. Based on this outcrop analysis, we choose the highest range of velocities to be the initial velocity model. After several tomographic iterations (Figure 12c), we obtain an improved, better focused subsurface image (Figure 12d). The black arrows indicate better illuminated, shallow, steeply dipping reflectors. The green arrow indicates a suite of previously poorly illuminated horizontal reflectors. The blue arrow shows that the shallow high-velocity part of the model significantly changes the depth and structural orientation of the deeper anticlinal target.

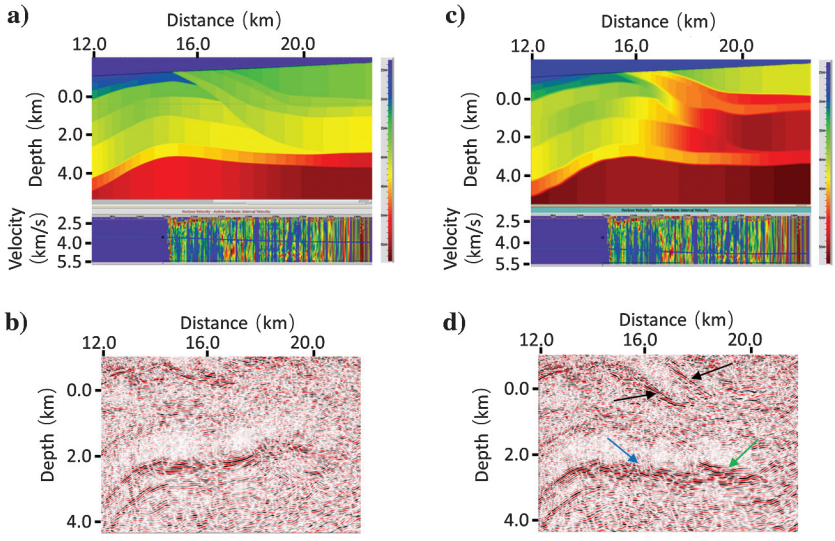

Figure 12. The importance of adding geologic constraints in building the velocity depth model for the overthrust example. (a) Velocity-depth model and (b) corresponding seismic image built using the seismic data alone. Seismically derived velocities are more accurate for intermediate depths, where the fold (more accurately, the number of illuminating raypaths) is high. Considering the geologic settings of this area, the overlying outcropped rocks behave very high velocity. The range of velocities that we choose is too low, and it makes the initial velocity model far from the correct one, so it is difficult for the tomography algorithm to converge. Incorporating this geologic information into the (c) update velocity depth model generates (d) an improved, better focused subsurface image. The black arrows indicate better illuminated shallow steeply dipping reflectors, the green arrow shows a suite of previously poorly illuminated horizontal reflectors, and the blue arrow shows that the higher shallow velocity significantly changes the depth and structural orientation of the deeper anticlinal target.

With the workflow presented in this paper, we evaluate the prestack depth-migration result in our research survey. Figure 13 shows the comparison of prestack time and depth migration. The prestack time-migration image (Figure 13a) is displayed in time, and the prestack depth-migration image (Figure 13b) is

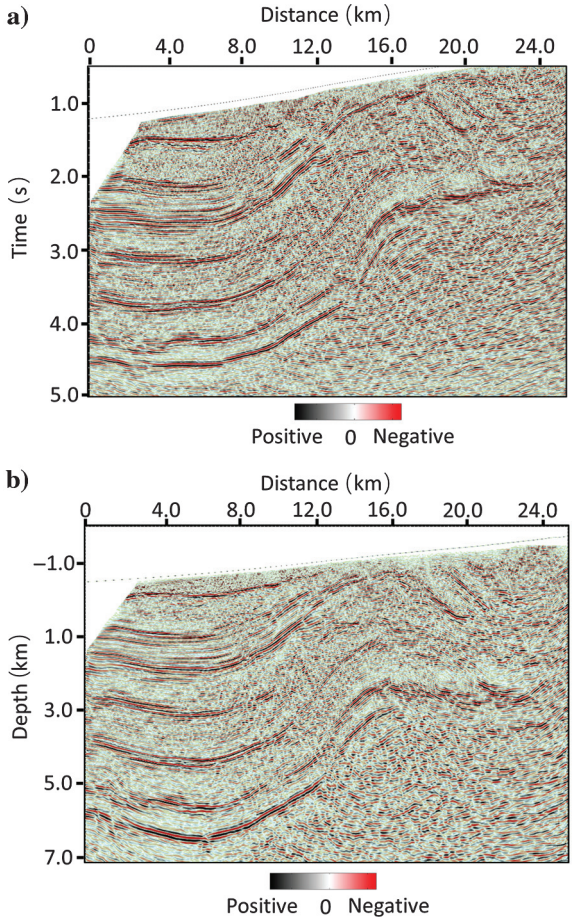

Figure 13. Comparison between prestack (a) time and (b) depth migration of the land survey with overthrust structures. Note the superior quality of the depth-migrated image compared with the time-migrated result. Specifically, the depth migration better images the faults and the steep dipping strata more clearly than time migration. There are also fewer migration artifacts (unfocused ellipses) in the depth imaging result. By examining differences in the strata underneath the overthrust structure, the time migration shows them dipping up to the right, whereas the depth migration shows them dipping down to the right, to avoid the velocity pull-up pitfall in time migration.

displayed in depth. Note the superior quality of the depth-migrated result (Figure 13b) compared with the time-migrated result (Figure 13a). Specifically, depth migration better images the faults and the steeply dipping strata more clearly than does time migration. There are also fewer migration artifacts (unfocused ellipses) in the depth imaging result. When examining differences in the strata underneath the overthrust structure, the time migration shows them dipping up to the right due to the velocity pull-up pitfall, whereas the depth migration shows them dipping down to the right. This velocity pull-up pitfall is common in time imaging beneath high-velocity overlying structures.

Conclusion

Imaging overthrust geologic structures is difficult for several reasons. First, overthrust terrains exhibit high lateral variations in velocity, requiring depth migration, and in turn an accurate velocity-depth model. Second, this lateral variation in geology occurs near the surface as well as at depth; the shallow section is often poorly illuminated, potentially resulting in erroneous estimates of the shallow velocity, thereby degrading all deeper images. In our example, we found that incorporating outcrop measurements provided a more accurate velocity-depth model and better subsurface images. Third, because older, more indurated rocks may lie near the surface, the seismic data may be contaminated by high-amplitude headwaves and other linear noise. Cascaded linear noise attenuation performed first on common-shot and then on common-receiver gathers effectively suppresses much of this noise, but it leaves aliased low-velocity components in the filtered images. These aliased components have shallow apparent dip and will overprint the subsequent migrated image. Overthrust terrains can exhibit rugose topography. We find that tomographic statics solutions provide significantly improved images over simple elevation corrections and conventional refraction statics solutions in the mountain area. Finally, tomographic velocity updating provides improved images over simpler residual velocity analysis techniques. The numerical tests on the synthetic overthrust model data and the field data in the Tuha Basin indicate that this paper's method could provide high-quality seismic images for the overthrust structures.

In summary, there is no simple solution to imaging overthrust geology. Appropriate modification and significant care at each step of the processing and imaging workflow to account for these particularly challenging imaging problem is necessary.

Acknowledgments

The authors would like to thank the sponsors of the Attribute-Assisted Seismic Processing and Interpretation (AASPI) consortium at the University of Oklahoma. We thank PetroChina Research Institute of Petroleum Exploration & Development-Northwest (NWGI) for permission to publish these results and for their commercial licenses of Paradigm's GeoDepth and WesternGeco Omega processing softwares. We also thank the three reviewers whose comments helped to improve and clarify this paper.

References

Alfonso, H., 2001, Seismic imaging and analysis over Colombian foothills: ACIPET.

Alfonso, H., and S. Guevara, 2004, Imaging over complex structures-Colombian Andes Case: 74th Annual International Meeting, SEG, Expanded Abstracts, 486–489.

Baysal, E., D. D. Kosloff, and J. W. C. Sherwood, 1983, Reverse-time migration: Geophysics, **48**, 1514–1524, doi: 10.1190/1.1441434.

Bell, M. L., R. Lara, and W. C. Gray, 1994, Application of turning-ray tomography to the offshore Mississippi

delta: 64th Annual International Meeting, SEG, Expanded Abstracts, 1509–1512.
Bleistein, N., 1987, On the imaging of reflectors in the earth: Geophysics, **52**, 931–942, doi: 10.1190/1.1442363.
Claerbout, J., 1971, Toward a unified theory of reflector mapping: Geophysics, **36**, 467–481, doi: 10.1190/1.1440185.
Dix, C. H., 1955, Seismic velocities from surface measurements: Geophysics, **20**, 68–86, doi: 10.1190/1.1438126.
Etgen, J., 1988, Velocity analysis using prestack depth migration: Linear theory: 58th Annual International Meeting, SEG, Expanded Abstracts, 909–912.
Etgen, J., S. H. Gray, and Y. Zhang, 2009, An overview of depth imaging in exploration geophysics: Geophysics, **74**, no. 6, WCA5–WCA17, doi: 10.1190/1.3223188.
Fagin, S., 1996, The fault shadow problem: Its nature and elimination: The Leading Edge, **15**, 1005–1013, doi: 10.1190/1.1437403.
Gray, S. H., J. Etgen, J. Dellinger, and D. Whitmore, 2001, Seismic migration problems and solutions: Geophysics, **66**, 1622–1640, doi: 10.1190/1.1487107.
Gray, S. H., and K. J. Marfurt, 1995, Migration from topography: Improving the near-surface image: Canadian Journal of Exploration Geophysics, **31**, 18–24.
Hémon, C., 1978, Equations d'onde et modèles: Geophysical Prospecting, **26**, 790–821.
Jiao, J., S. Trickett, and B. Link, 2004, Wave-equation migration of land data: CSEG National Convention, Extended Abstracts, 1–2.
Marfurt, K. J., and B. Duquet, 1999, Mapping prestack depth migrated coherent signal and noise events back to the original time gathers using Fermat's principle: Geophysics, **64**, 934–941, doi: 10.1190/1.1444601.
McMechan, G. A., 1983, Migration by extrapolation of time-dependent boundary values: Geophysical Prospecting, **31**, 413–420, doi: 10.1111/j.1365-2478.1983.tb01060.x.
Osypov, K., 1998, A comparative study between 3-D diving-wave tomography and head-wave refraction methods: 68th Annual International Meeting, SEG, Expanded Abstracts, 1222–1225.
Reshef, M., 1991, Depth migration from irregular surfaces with depth extrapolation methods: Geophysics, **56**, 119–122, doi: 10.1190/1.1442947.
Ristow, D., and T. Ruhl, 1994, Fourier finite-difference migration: Geophysics, **59**, 1882–1893, doi: 10.1190/1.1443575.
Ritchie, W., M. Popovici, M. Fleidner, and C. Saxon, 2005, Challenges and opportunities in pre-stack depth imaging of legacy seismic data: An overthrust belt case study: 75th Annual International Meeting, SEG, Expanded Abstracts, 400–404.
Schneider, W. A., 1978, Integral formulation for migration in two and three dimensions: Geophysics, **43**, 49–76, doi: 10.1190/1.1440828.
Schneider, W. A., and S. Kuo, 1985, Refraction modeling for static corrections: 55th Annual International Meeting, SEG, Expanded Abstracts, 295–299.
Shan, G., L. Zhang, Y. Wang, T. Nemeth, and W. Liu, 2008, Velocity sensitivity of reverse-time migration: 78th Annual International Meeting, SEG, Expanded Abstracts, 2321–2325.
Shragge, J., 2005, Wave equation migration from topography: Imaging Husky: Stanford Exploration Project, Report 123, 49–56.
Spitz, S., 1991, Seismic trace interpolation in the f-x domain: Geophysics, **56**, 785–794, doi: 10.1190/1.1443096.
Stoffa, P. L., J. T. Fokkema, R. M. de Luna Freire, and W. P. Kessinger, 1990, Split-step Fourier migration: Geophysics, **55**, 410–421, doi: 10.1190/1.1442850.
Stork, C., 1992, Reflection tomography in the postmigrated domain: Geophysics, **57**, 680–692, doi: 10.1190/1.1443282.
Taner, M. T., F. Koehler, and K. A. Alhilali, 1974, Estimation in correction of near-surface time anomaly: Geophysics, **39**, 441–463, doi: 10.1190/1.1440441.
Taner, M. T., D. E. Wagner, E. Baysal, and L. Lu, 1998, A unified method for 2-D and 3-D refraction statics: Geophysics, **63**, 260–274, doi: 10.1190/1.1444320.
Vermeer, G., 1991, Symmetric sampling: The Leading Edge, **10**, 21–27, doi: 10.1190/1.1436788.
Wang, X., Y. Wang, X. Wang, W. Liu, Q. Su, B. Lyu, and Y. Tian, 2012, Methods and application for relative fidelity processing of seismic data (in Chinese): Petroleum Industry Express.
Whitmore, D. N., 1983, Iterative depth imaging by back time propagation: 53rd Annual International Meeting, SEG, Expanded Abstracts, 382–386.
Yilmaz, O., 1987, Seismic data processing: SEG.
Yilmaz, O., 2001, Seismic data analysis: SEG.
Zhang, Y., G. Zhang, and N. Bleistein, 2005, Theory of true amplitude one-way wave equations and true amplitude common-shot migration: Geophysics, **70**, no. 4, E1–E10, doi: 10.1190/1.1988182.
Zhou, B., and S. A. Greenhalgh, 1994, Wave-equation extrapolation-based multiple attenuation: 2-D filtering in the f-k domain: Geophysics, **59**, 1377–1391, doi: 10.1190/1.1443696.
Zhu, X., B. G. Angstman, and D. P. Sixta, 1998, Overthrust imaging with tomo-datuming: Geophysics, **63**, 25–38, doi: 10.1190/1.1444319.
Zhu, X., D. P. Sixta, and B. G. Angstman, 1992, Tomostatics: Turning-ray tomography + static correction: The Leading Edge, **11**, 15–23, doi: 10.1190/1.1436864.

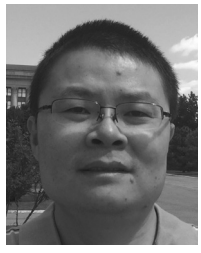

Bin Lyu received a B.S. (2003) and an M.S. (2006) in exploration geophysics from the China University of Petroleum. He is pursuing a Ph.D. in geophysics from the University of Oklahoma as a member of the AASPI Consortium. From 2006 to 2015, he served as a geophysicist in the Petrochina Research Institute of Petroleum

Exploration and Development-Northwest. His research interests include seismic processing, seismic migration, migration velocity analysis, and seismic attributes.

Qin Su received a bachelor's degree (1999) from Jianghan Petroleum University. After graduation, he joined PetroChina Research Institute of Petroleum Exploration and Development-Northwest (NWGI) and served as a geophysicist. His research interests include seismic processing and prestack migration.

Kurt J. Marfurt received a Ph.D. (1978) in applied geophysics at Columbia University's Henry Krumb School of Mines in New York. He joined The University of Oklahoma in 2007, where he serves as the Frank and Henrietta Schultz Professor of Geophysics within the ConocoPhillips School of Geology and Geophysics. He worked for 18 years in a wide range of research projects at Amoco's Tulsa Research Center, after which he joined the University of Houston for eight years as a professor of geophysics and the director of the Allied Geophysics Lab. He teaches short courses on attributes for SEG and AAPG and serves as editor of *Interpretation*. His research includes prestack imaging, velocity analysis and inversion, 5D seismic data interpolation, computer-assisted pattern recognition of geologic features on 3D seismic data, and interpreter-driven seismic processing. His research interests include seismic signal analysis, 3D seismic attributes, seismic velocity analysis, subsurface imaging, and multicomponent data analysis.